

Supporting Information

Assembly and PhotocARRIER Dynamics of Heterostructured Nanocomposite Photoanodes from Multicomponent Colloidal Nanocrystals

Anna Loiudice,^{a,b} Jason K. Cooper,^{a,b} Lucas H. Hess,^{a,b} Tracy Mattox,^c Ian D. Sharp^{a,d*} and R. Buonsanti^{a,b*}

^aJoint Center for Artificial Photosynthesis, Lawrence Berkeley National Laboratory, One Cyclotron Road, Berkeley, California 94720, United States.

^bMaterials Science Division, Lawrence Berkeley National Laboratory, One Cyclotron Road, Berkeley, CA 94720, United States.

^cThe Molecular Foundry, Lawrence Berkeley National Laboratory, One Cyclotron Road, Berkeley, CA 94720, United States.

^dChemical Sciences Division, Lawrence Berkeley National Laboratory, One Cyclotron Road, Berkeley, CA 94720, United States.

Experimental Details

Materials. Bismuth (III) Chloride (98%) (BiCl_3), Vanadyl Acetylacetonate (99.99%) ($\text{VO}(\text{acac})_2$), Tungsten (IV) Chloride (WCl_4), Tungsten (V) Ethoxide (94%), Titanium Tetrachloride, Titanium(IV) isopropoxide (97%), Trimethylamine N-Oxide (98%), 1-Octadecene (technical grade, 90%), Oleic acid (technical grade, 90%) (OLAC), Oleylamine (technical grade, 70%) (OLAM), Trioctylamine (98%), were purchased from Aldrich and used without further purification.

$\text{Bi}_2\text{O}_{2.7}/\text{VO}_x$ synthesis. 3.17 mmol of BiCl_3 was dispersed in 10 mL of OLAM in a 25 mL three-necked flask equipped with a condenser and a thermocouple held by a glass tube. The solution was continuously stirred and kept under vacuum for 1h. The solution was then heated to 170 °C in the course of 15 min and then kept at that temperature for 1 h. During this whole time it was necessary to keep a flow of N_2 through the flask in order to obtain best results. After this time the color of the BiCl_3 solution turned from milk white to dark gray. A solution of 1.27 mmol of $\text{VO}(\text{acac})_2$ in 1 mL of OLAM was then swiftly injected into the flask. The solution turned black after injection and the nanocrystals were allowed to grow for 30 min at 250 °C. The reaction was then quenched with cold hexane. Unsolubilized materials were removed by centrifugation, and ethanol was added dropwise to the supernatant until it became turbid. The mixture was centrifuged, the supernatant discarded, and the precipitated nanoparticles redispersed in hexane.

TiO₂ nanorods (TiO₂-small) synthesis. TiO₂-small were obtained following the procedure reported by *D. P. Cozzoli et al.*¹ 15 mmol of titanium(IV) isopropoxide were dissolved in 70 g of degassed OLAC and the resulting solution was then reacted with 5 mL of an aqueous 2 M trimethylamine N-oxide solution at 100 °C for 96 h.

TiO₂ branched nanocrystal (TiO₂-big) synthesis. TiO₂-big were obtained following the procedure reported by *R. Buonsanti et al.*² 3 g of 1-octadecene, 3 mmol of OLAM and 11 mmol of OLAC were loaded in a three-neck flask and degassed at 120 °C for 45 min, after which the mixture is cooled down to 50 °C under N₂ flow. At this point, 1 mmol of titanium tetrachloride dissolved in 1 mL of 1-octadecene was added and the flask was heated up to 290 °C at a ramp rate of 25 °C min⁻¹. After heating for 1 h at 290 °C, the reaction was stopped.

WO₃ nanorods aspect ratio 2 (WO₃-small) synthesis. The synthesis of WO₃-small was carried out by adapting a procedure reported by *T. Mattox et al.*³ 66 mg of WCl₄, 1.2 ml OLAM, and 3.5 ml OLAC were stirred at 300°C for 120 min under nitrogen. After that the solution was cooled at room temperature.

WO₃ nanorods aspect ratio 12 (WO₃-big) synthesis. The synthesis of WO₃-big was carried out by adapting a procedure reported by *K. Manthiram et al.*⁴ 12.5 ml OLAC and 17.5 ml of trioctylamine were degassed at 150°C for 1h. The flask was then placed under nitrogen and heated at 335°C for 3h. The solution was then cooled at 315°C and 0.5 ml of tungsten (V) ethoxide was rapidly injected. The reaction was held at 315°C for 5 min and then cooled at room temperature.

Nanocrystal (NC) solutions and films characterization:

Low and high resolution transmission electron microscopy (TEM) was carried out on JOEL 2100 and a JOEL 2100F microscopes, respectively, both operating at 200 kV. The latter was used also for high-angle annular dark field scanning TEM (HAADF-STEM). Energy dispersive X-ray (EDX) analysis was performed on the JOEL 2100F with a liquid nitrogen-cooled Oxford Instruments INCA-EDS detector. Samples were prepared by drying a drop of hexane solution containing the NCs on the surface of a carbon-coated copper grid or a silicon nitride membrane window (Ted Pella, Inc.).

Elemental analysis was performed by ICP-AES with a Varian 720/730 Series spectrometer. The NC samples were digested by solution and films in concentrated HNO₃. The relative error on the extracted Bi and V was within 3%, as evaluated on the basis of 5 replicates per each measurement.

Wide-angle XRD was performed using a Bruker D8-Advanced X-ray diffractometer equipped with a GADDS area detector operating at Cu-K α wavelength of $\lambda = 1.54 \text{ \AA}$. Samples were prepared by drop casting NCs on silicon substrates.

X-ray photoelectron spectroscopy (XPS) was performed using a monochromatized Al K α source ($h\nu = 1486.6 \text{ eV}$), operated at 225 W, on a Kratos Axis Ultra DLD system at a takeoff angle of 0° relative to the surface normal and a pass energy for narrow scan spectra of 20 eV, corresponding to an instrument resolution of approximately 600 meV. Survey spectra were collected with a pass energy of 80 eV. Spectral fitting was performed using CASA analysis software. Spectral positions were corrected by shifting the primary C 1s core level position to 284.8 eV, and curves were fit with quasi-Voigt lines following Shirley background subtraction. Samples were deposited on conductive silicon substrates.

Scanning electron microscopy (SEM) images were recorded on a Zeiss Gemini Ultra-55 Analytical Scanning Electron Microscope using beam energy of 10 kV and an In-Lens detector. Samples were spin coated on a silicon substrate prior to imaging.

UV–Vis diffuse reflectance spectra were recorded on a Shimadzu SolidSpec-3700 spectrometer with a D₂ (deuterium) lamp for the ultraviolet range and a WI (halogen) lamp for the visible and near infrared. Measurements were performed with an integrating sphere. Samples were deposited on quartz substrates.

Raman spectroscopy measurements were performed using a Horiba Yvon Jobin LabRAM HR confocal Raman microscope with a laser excitation wavelength of 532 nm and a power of 0.1-0.3 mW at the objective (spot size of approximately 1 μm).

Transient absorption spectroscopy was conducted on monocrystalline BiVO₄ samples which were spin coated onto quartz substrates. The pump beam was produced by a Coherent Libra (Coherent, CA, USA) laser coupled to a Coherent OPerA Solo optical parametric amplifier (OPA). The output was directed to the sample as the excitation pump, with a wavelength of 350 nm, pulse duration of 150 fs, repetition rate of 1 kHz, pulse energy of 700 nJ, and beam diameter of 0.3 mm at the sample. The transient absorption system was produced by Ultrafast Systems and contained a probe laser produced by Leukos (Leukos Systems, France) with a pulse width < 1 ns and broad band emission, detected with a grating spectrometer coupled to a Si CMOS detector array for analysis in the ~400-800 nm spectral range. The differential absorption was collected as a function of pump probe delay through accumulated random sampling of electronically triggered delay times.

The decay traces were fit with a double exponential plus a stretched exponential equation, as given by:

$$dA(t) = A_1 \exp(-x/\tau_1) + A_2 \exp(-x/\tau_2) + A_3 \exp(-(x/\tau_3)^\alpha) \quad (S1)$$

where A_i and τ_i represent the initial amplitude and the lifetime of the i^{th} component and α is the stretching parameter, included to account for a broad population distribution of trap states; α for all samples was fixed to 0.5, which provided an adequate fit of the longer tailing portion of the transient response. A 15% error on the lifetimes is typical from this type of analysis.

For the ms-s TAS, the samples were pumped with 355nm laser at a repetition rate of 1 Hz and a power of 4mJcm⁻² generated by a Minilite II system (Continuum, USA). For probing, the 550nm component of the light produced by a quartz tungsten halogen lamp (250W, Newport Corporation, USA) was selected with a CS260 monochromator (Newport Corporation, USA). The light transmitted through the sample was detected by a Si avalanche photodetector (APD120A2, Thorlabs Inc., USA). To filter unwanted stray light, the photodiode was mounted at the exit of a MS257 monochromator (Newport Corporation, USA) set to 550nm. The diode signal was amplified by a low noise voltage preamplifier (SR560, Stanford Research Systems Inc., USA) and recorded with a DPO4054 oscilloscope (Tektronix Inc., USA) triggered with respect to the laser pulses. 2500 transients were recorded and averaged for each measurement. Finally, the data was averaged logarithmically in time.

Electrode preparation and photoelectrochemical measurements. Electrodes were prepared by spin coating Bi₂O_{2.7}@VO_x NC heterodimers dispersed in hexane on FTO-coated glass substrates (~ 1 x 1 cm) at 700 rpm for 45 s. The obtained films appeared very shiny with a thickness of around 100 nm. Next,

the films were annealed in air inside a tube furnace at 350 °C for 2 hr or 500 °C for 10 min. Excess of V₂O₅ present in the BiVO₄ electrodes was removed by soaking them in 1M NaOH solution for 30s with gentle stirring. The resulting pure BiVO₄ electrodes were rinsed with DI water and dried. Photoelectrochemical performance characteristics of photoanodes were evaluated in a typical undivided three-electrode configuration using a CHI 604D Potentiostat/Galvanostat. The light source was an AM 1.5 solar simulator (Solar Light Co, Inc. model XPS 300) with the illumination intensity adjusted to 100 mW/cm². All illuminated areas were approximately 0.2 cm². Photocurrent measurements were performed in a 1 M potassium phosphate buffer solution (pH 6.8) with 0.1 M sodium sulfite (Na₂SO₃) as a hole scavenger. Photocurrents were monitored either while sweeping the potential to the positive direction with a scan rate of 10 mV/s. While all measurements were carried out using a Ag/AgCl (4M KCl) reference electrode, all results in this work were presented against the reversible hydrogen electrode (RHE) for ease comparison with other papers that use electrolytes with different pH conditions. The conversion between potentials vs. Ag/AgCl and vs. RHE is performed using the following equation 1:

$$E(\text{vs. RHE}) = E(\text{vs. Ag/AgCl}) + E_{\text{Ag/AgCl}}(\text{reference}) + 0.0591\text{V} \times \text{pH}$$

$$E_{\text{Ag/AgCl}}(\text{reference}) = 0.1976\text{ V vs. NHE at } 25\text{ }^{\circ}\text{C}$$

A set of 5 photoelectrodes was tested for each studied structure.

Incident photon-to-charge conversion efficiency (IPCE) was measured using an home built setup. A Newport 150W Xe lamp and an Oriel Cornerstone 1/8m monochromator with 1.5 nm slits, yielding a spectral resolution of better than 0.5 nm was used as a light source. A beam splitter, together with a Thorlabs FDS1010-CAL calibrated Si photodiode, was used to monitor the intensity of the monochromatic output during the measurement. In order to ensure accurate measurement, the incident light spot under-filled both the sample and reference diode. A Gamry Reference 600 potentiostat was used in combination with a three-electrode electrochemical cell to maintain the sample at the reported potentials and to measure the current of the photoanode. The IPCE was then calculated based on the following formula:

$$IPCE(\%) = \frac{1240 \times J_{ph}}{I_i \times \lambda} \times 100 \quad (2)$$

where J_{ph} is the measured photocurrent density in mA/cm², I_i is the incident light intensity in mW/cm², and λ is the incident photon wavelength in nm.

Photocurrent density obtained for sulfite oxidation was used to calculate the charge separation efficiency (ϕ_{sep}) by using Eq. 3,

$$J_{PEC} = J_{max} \times \eta_{LHE} \times \phi_{sep} \times \phi_{ox} \quad (3)$$

where J_{PEC} is the measured photocurrent density, J_{max} is the maximum photocurrent density achievable assuming 100% IPCE for photons with energy $\geq E_g$, η_{LHE} is the light harvesting efficiency and ϕ_{ox} is the surface transfer efficiency. For sulfite oxidation with extremely fast oxidation kinetics, surface recombination is negligible, and ϕ_{ox} is ~ 1 . Therefore, ϕ_{sep} is obtained by dividing J_{PEC} by $J_{max} \times \eta_{LHE}$. In order to calculate J_{max} of the nanocomposite samples used in this work, the National Renewable Energy Laboratory (NREL) reference solar spectral irradiance at AM 1.5G (radiation energy (Wm⁻²nm⁻¹) vs. wavelength (nm)) was first converted to the solar energy spectrum in terms of number of photons (s⁻¹m⁻²nm⁻¹) vs. wavelength (nm). Then, the number of photons above the band gap energy of the samples analyzed was calculated using a trapezoidal integration (10 nm increments). The η_{LHE} is calculated at each wavelength using the following equations: $\eta_{LHE} = 1 - 10^{-A(\lambda)}$ where $A(\lambda)$ is the absorbance at wavelength λ . $J_{max} \times \eta_{LHE}$ of the BiVO₄, BiVO₄/WO₃-small and BiVO₄/WO₃-big was calculated to be 5.38, 4.65 and 4.80 mA/cm² respectively.

By dividing J_{PEC} (measured at 1.23 V vs. RHE) by $J_{max} \times \eta_{LHE}$, ϕ_{sep} of 12%, 28% and 24% are obtained for BiVO₄, BiVO₄/WO₃-small and BiVO₄/WO₃-big respectively.

Nanocomposite electrode preparation. First, different nanocomposite mixtures were prepared by mixing the MOs with Bi₂O_{2.7}/VO_x heterodimers (both in hexane solution) in a weight ratio of 1:1. The as prepared mixtures were kept in stirring for 2 h to ensure a good mixing. After that the electrodes were fabricated using a layer-by-layer technique. One drop of nanocomposite solution was spin-coated at 700 rpm for 45 s. The film was then annealed at 500°C for 10 min. The sequence was repeated to achieve a film thickness of 200 nm.

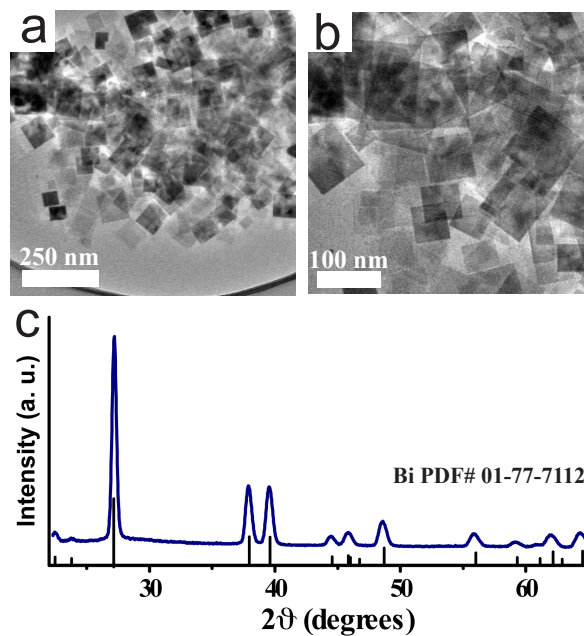


Figure S1. (a, b) Low resolution TEM images at different magnitude and (c) XRD pattern of the product obtained after reaction of the BiCl_3 with oleylamine at $170\text{ }^\circ\text{C}$ for 1 h. The obtained Bi NCs possessed a nanosheet shape with an average size of ca. 100 nm. The XRD pattern showed the characteristic peaks of elemental bismuth (JCPDS #01-77-7112).

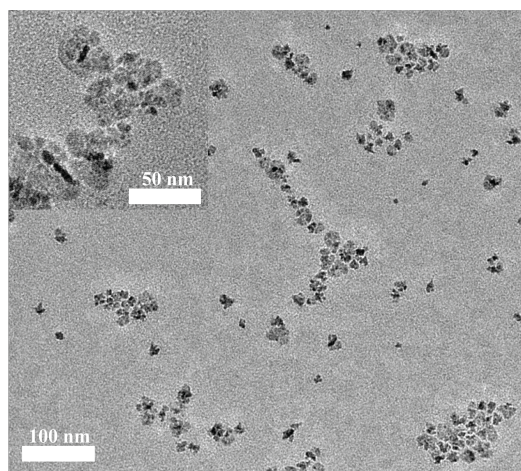


Figure S2. TEM images at different magnitude of the $\text{Bi}_2\text{O}_{2.7}/\text{VO}_x$ NC heterodimers obtained when the bismuth and vanadium precursors were introduced simultaneously at the beginning of the synthesis.

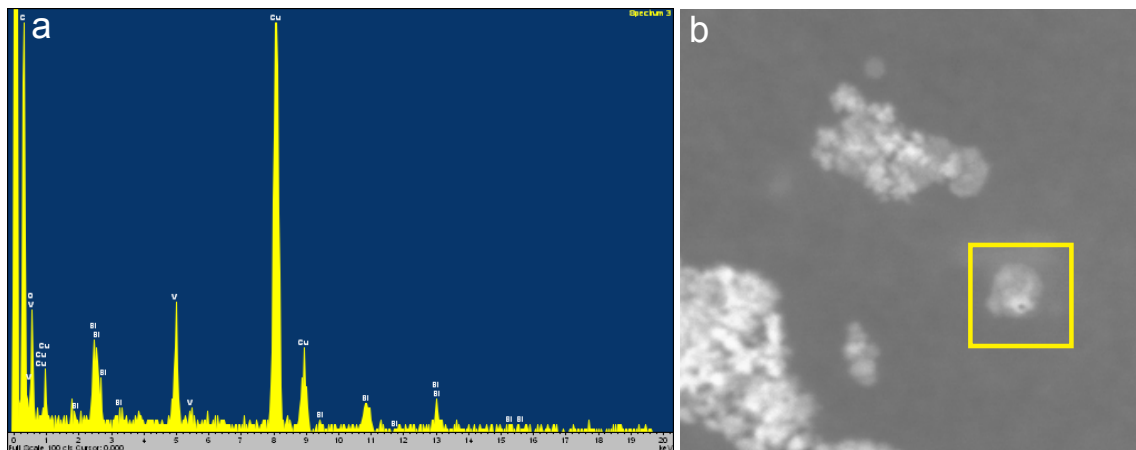


Figure S3. (a) Representative STEM-EDS spectrum of $\text{Bi}_2\text{O}_{2.7}/\text{VO}_x$ NC heterodimers area corresponding to the region enclosed by yellow box in (b). The Cu signals were attributed to the Cu TEM grid. The spectrum acquired on an area without any nanoparticles showed the EDS spectrum of the only Cu. The quantification of the Bi and V was not possible due to the overlap between the oxygen peaks and the vanadium ones at lower keV.

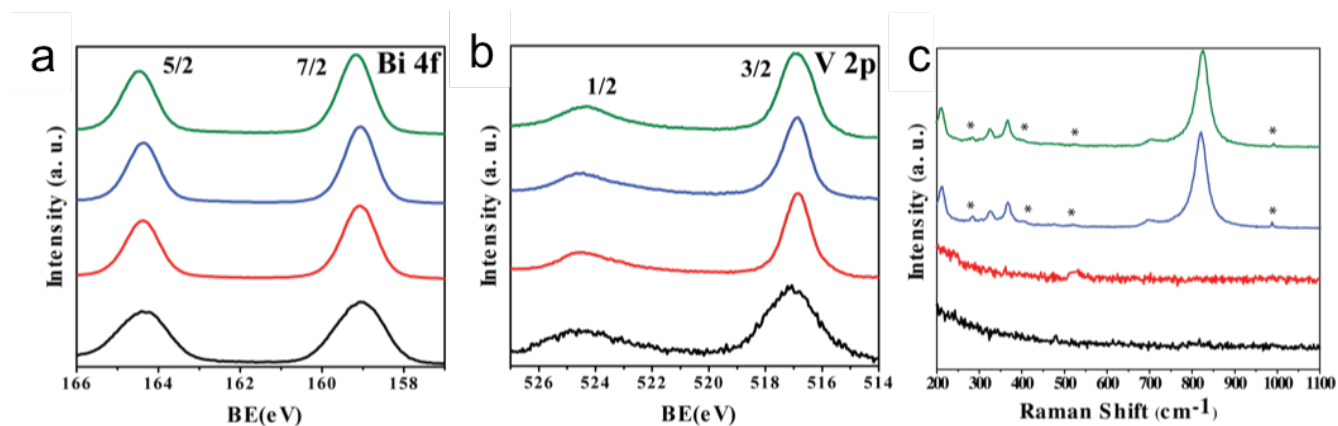


Figure S4. High resolution XPS spectra of the Bi 4f (a) and V 2p (b) core level regions and Raman spectra (c) from the $\text{Bi}_2\text{O}_{2.7}/\text{VO}_x$ NC heterodimer films annealed at different temperatures: room temperature (black line), 250 °C (red line), 350 °C (blue line) and 500 °C (green line). The Bi 4f_{7/2} peak of each XPS spectrum was fitted with a peak centered at 159.1 eV that can be assigned to oxidation state +3. The presence of Bi in the elemental oxidation state is not detectable in any sample. Also the analysis of the V 2p_{3/2} peak revealed that only one spectral component centered at 517.3 eV fitted well all the spectra resulting in an oxidation state of +5. Calculation of the surface atomic composition performed using total V 2p_{3/2}, Bi 4f_{7/2} and Bi 4f_{3/2} spectral intensities, weighted by the corresponding atomic

sensitivity factors of more than five samples, yielded an average composition ratio of V/Bi of 1.4, in excellent agreement with the reported ICP results. The Raman spectra of the samples at room temperature and annealed at 250 °C did not show any characteristic peaks, probably because the crystalline domains were embedded in an optically absorbing amorphous matrix. This result was in accordance with the very broad peaks and intense background observed during the XRD analysis (see manuscript) for the samples at room temperature and annealed at 250°C. Raman bands around 210, 324, 366, 640, 710 and 826 cm^{-1} were observed for the samples annealed at 350 °C and 500 °C, which correspond to the typical vibrational bands of BiVO_4 . Moreover, the broad features indicated with * symbol observed for the samples annealed at 350°C and 500°C, matched the frequencies of the Raman-active vibrational modes of V_2O_5 ,⁵ and were consistent with the excess of vanadium found with the ICP and XPS analysis.

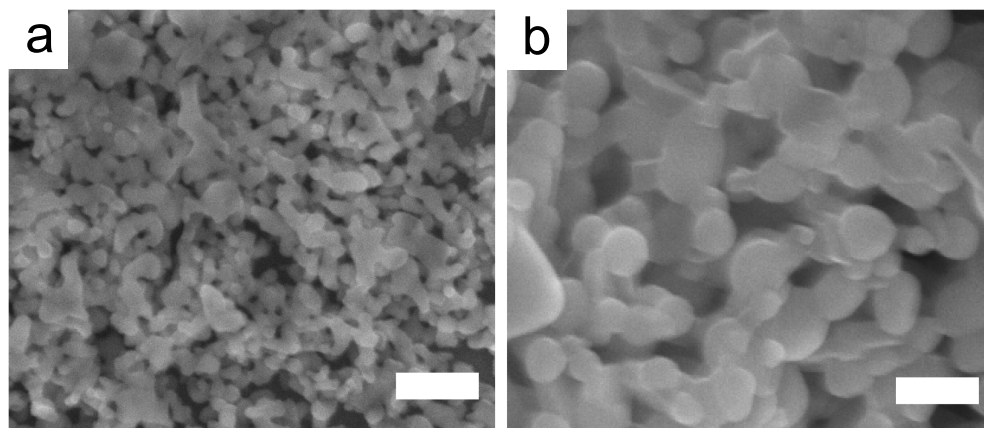


Figure S5. (a) SEM image of spin-coated films annealed at (a) 350 °C for 2h and (b) 500 °C for 10 min. Scale bars are 100 nm.

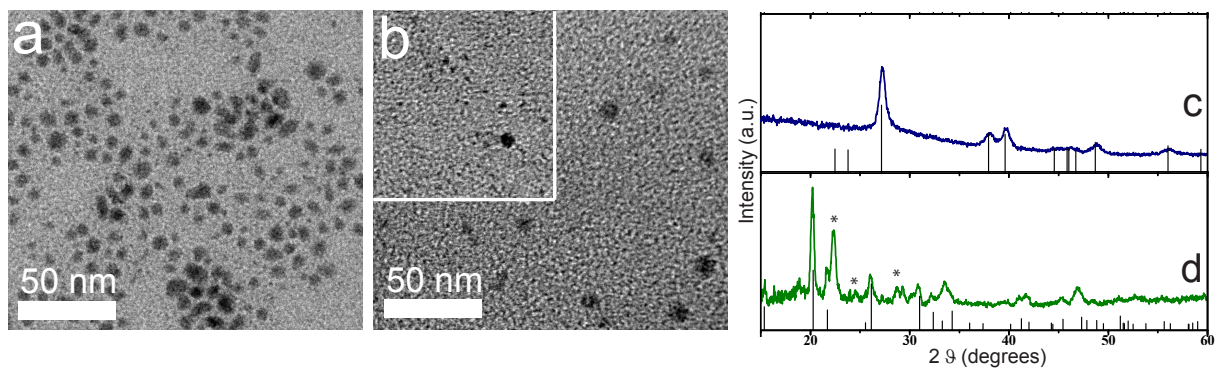


Figure S6. TEM images of (a) Bi NCs obtained following the synthesis reported by Talapin et al.⁶ and (b) the product obtained by using the pre-synthesized Bi NCs shown in **a** as nucleation seeds for the VO_x domains. The followed synthetic procedure was the same described in the manuscript but the Bi NCs were used instead of the BiCl₃ precursor. The scale bar of the inset is 25 nm. Homogeneous nucleation of unidentified small nanoparticles of around 2-3 nm occurred during the synthesis in the presence of Bi NCs while the latter remained unchanged after the synthesis.

XRD patterns of (c) as-synthesized sample in **b** and (d) after annealing of the same at 500°C for 10 min. The XRD of the as-synthesized sample did not appear to be different from that of the as-synthesized Bi NCs (JCSPD #01-071-4642). After annealing, the V₂O₅ phase (JCSPD #00-041-1426) was present together with an impurity phase (*) that cannot be indexed to any known phase. This result underlined the importance of the presence of Bi, V and O within the same NC building blocks in order to obtain the *m*-BiVO₄ phase.

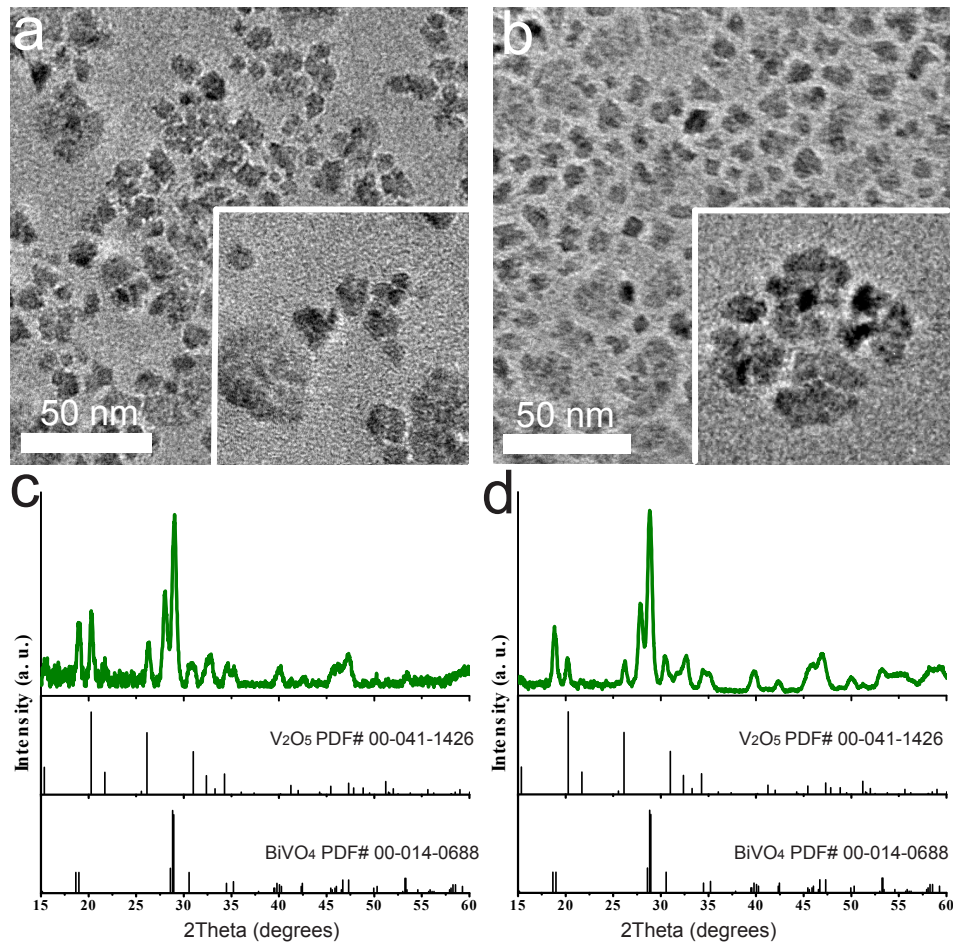


Figure S7. TEM images of NCs made with different Bi and V precursors molar ratio Bi:V (a) 1:1 (1.27:1.27 mmol) and (b) 1:2 (0.60:1.27 mmol). The NC heterodimer morphology and size appeared similar to those discussed in the manuscript. However, in these samples we only observed NCs composed of by flower-like amorphous VO_x nanoparticles. The XRD patterns after annealing at 500 °C for 10 min of the same samples reported in (c) and (d) respectively, showed that the *m*-BiVO₄ phase is present together with the V₂O₅ orthorhombic phase.

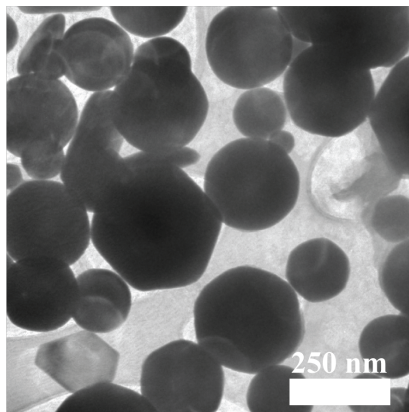


Figure S8. TEM image of the product obtained with the synthesis carried out with precursor molar ratio Bi:V = 3:1 (6.34: 1.27 mmol).

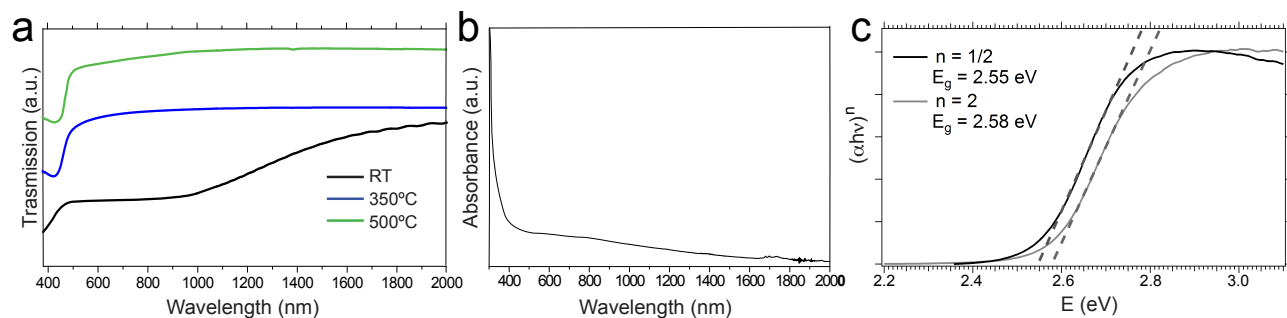


Figure S9. (a) UV-Vis spectrum in film of the as-deposited NCs (black line), annealed at 350 °C (blue line) and annealed at 500 °C (green line). (b) UV-Vis spectrum in solution of the as-synthesized heterodimers suspended in tetrachloroethylene. (c) Tauc plots indicating the direct and indirect bandgap energies of the film annealed at 500 °C.

The as-deposited films showed two absorption onsets at 400 nm and 1500 nm, corresponding to band gaps of 2.6 eV and 0.8 eV, respectively. These absorption features cannot be unequivocally attributed due to the complexity of Bi-O and V-O systems; however, the larger band gap is consistent with one of the different existing phases of the Bi-O family ($E_g = 2.29$ eV - 3.31 eV for BiO, α -Bi₂O₃, Bi₂O₃) and the smaller one with the presence of VO_x.^{7,8}

Our Tauc analysis in Figure S9c indicates a linear dependence of $(\alpha h\nu)^n$ vs energy with both $n=1/2$ (indirect band gap) and $n=2$ (direct band gap), therefore no conclusion on the exact nature of the band gap can be made on the basis of this sole measurement. There is some discussion in the literature as to

whether the lowest band gap of *m*-BiVO₄ is direct or indirect. Recent experimental papers report that *m*-BiVO₄ has a direct bandgap between 2.4 to 2.5eV.^{9,10} However, other recent theoretical work together with our recent results on BiVO₄ films synthesized with different methods,¹¹⁻¹³ where resonant inelastic x-ray scattering measurements complement UV-Vis data, clearly demonstrate that *m*-BiVO₄ is an indirect bandgap material with the direct bandgap of slightly larger energy.



Figure S10. Photographs of the (a) as-synthesized Bi₂O_{2.7}/VO_x NC heterodimers suspended in hexane and (b) spin-coated on quartz substrate and annealed at different temperatures (from left to right: room temperature, 250°C, 350° and 500°C).

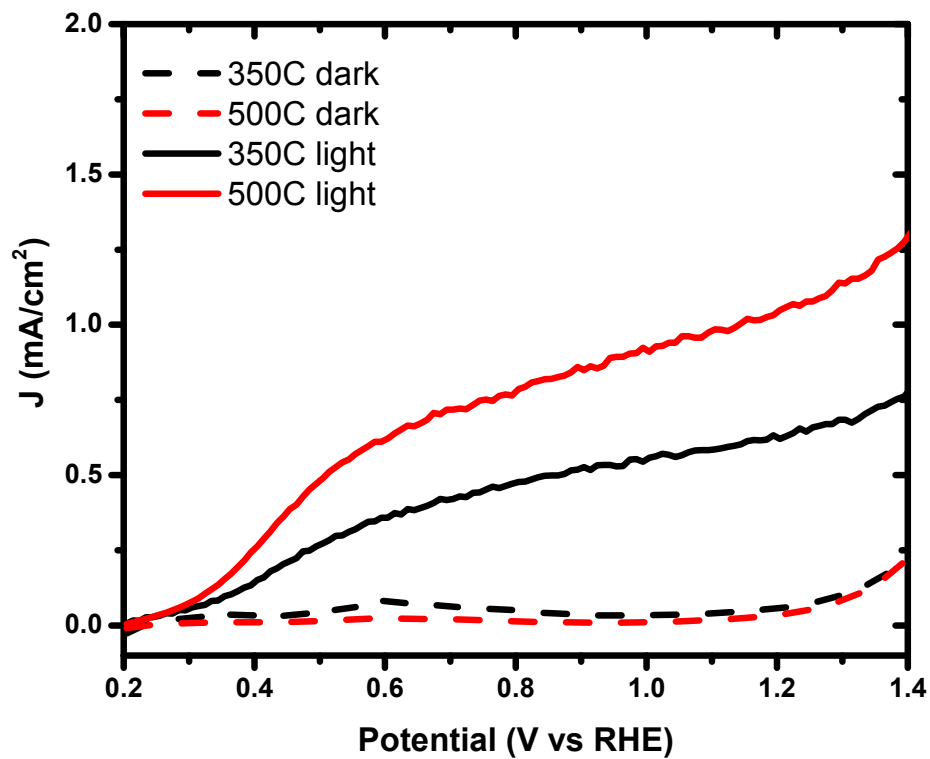


Figure S11. Current density vs. voltage (J-E) curves of photoelectrodes prepared from $\text{Bi}_2\text{O}_{2.7}/\text{VO}_x$ NC heterodimers annealed at 350 °C (black line) and 500°C (red line) measured under illumination (continuous traces) and in dark (dashed traces) in a 1 M phosphate buffer (pH 6.8) containing 0.1 M Na_2SO_3 as hole scavenger.

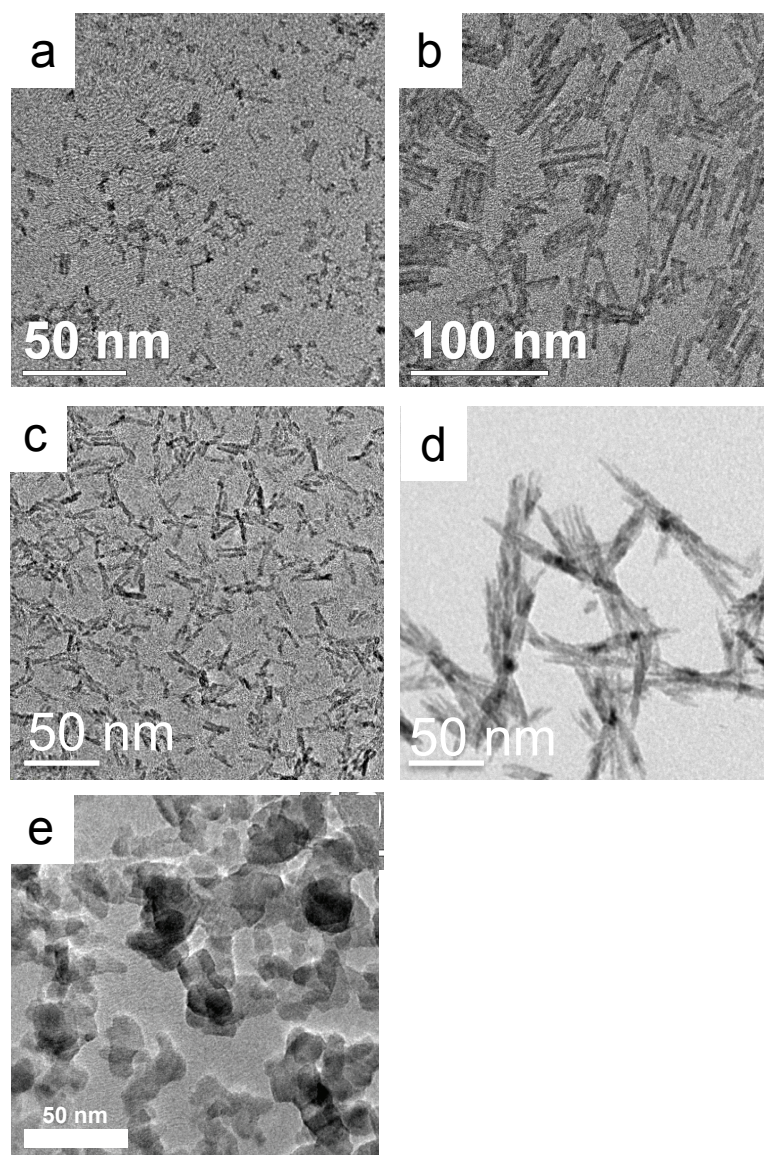


Figure S12. TEM images of different MOs used: (a) WO_3 -small, (b) WO_3 -big, (c) TiO_2 -small, (d) TiO_2 -big, and (e) Al_2O_3 nanoparticles purchased by Aldrich (20 wt. % in isopropanol).

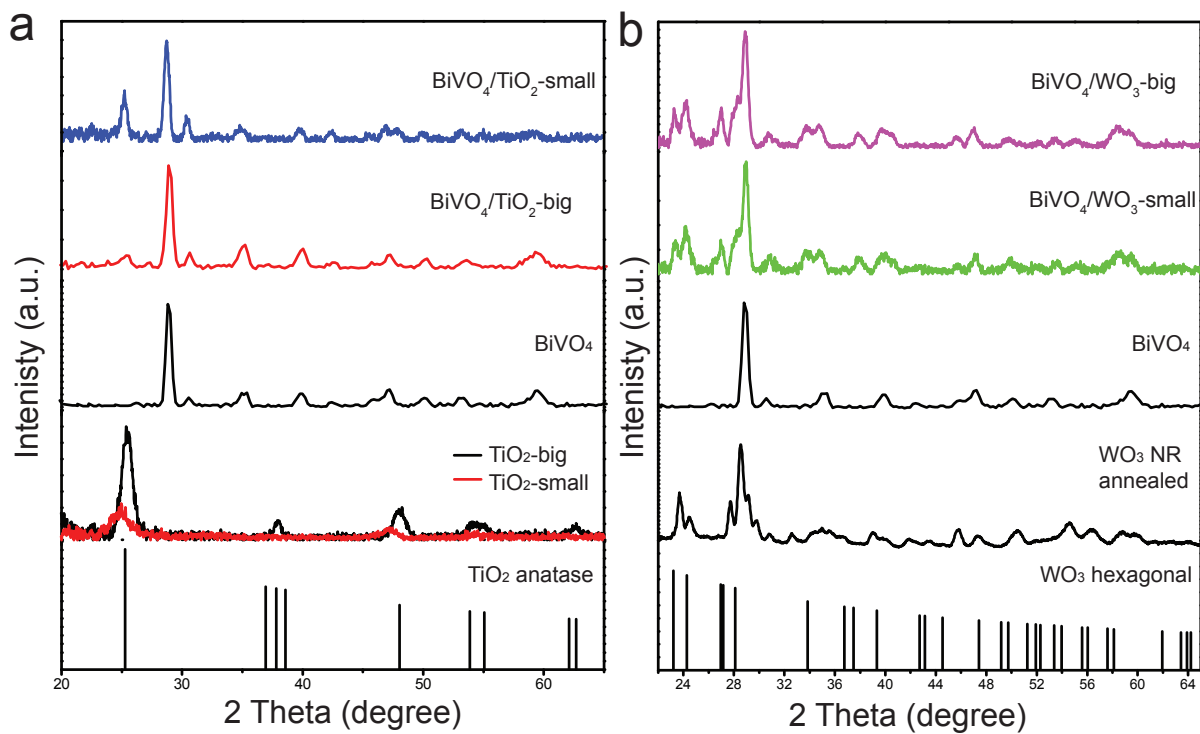


Figure S13. XRD spectra of (a) BiVO₄/TiO₂-small and BiVO₄/TiO₂-big and (b) BiVO₄/WO₃-small and BiVO₄/WO₃-big nanocomposites compared with the XRD spectra of bare BiVO₄, bare TiO₂-small, TiO₂-big and bare WO₃ annealed NR. TiO₂ anatase and WO₃ hexagonal phase references are reported on the bottom of each graph.

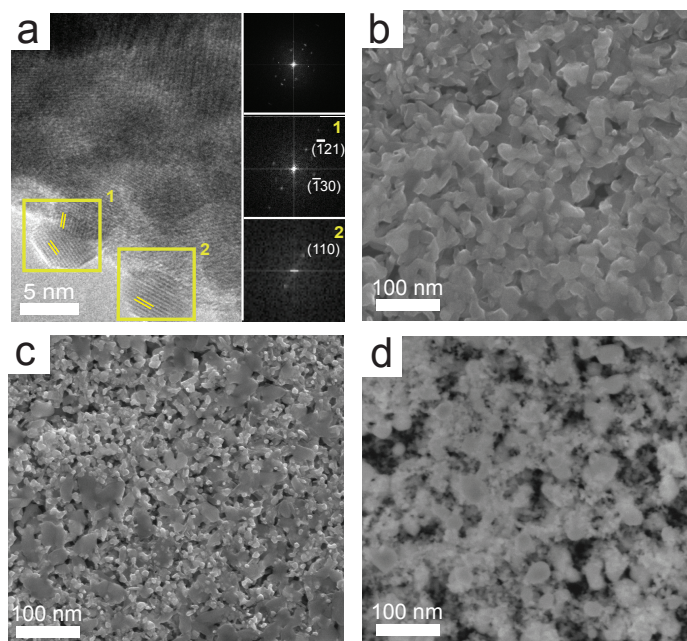


Figure S14. (a) HR-TEM image of BiVO₄, along with the FFTs from the corresponding regions enclosed by labeled yellow boxes (right). (b), (c) and (d) surface SEM images of the BiVO₄/WO₃-small, BiVO₄/TiO₂-small and BiVO₄/Al₂O₃ nanocomposites respectively. EDS analysis was used to verify the weight ratio BiVO₄:MO in the nanocomposites.

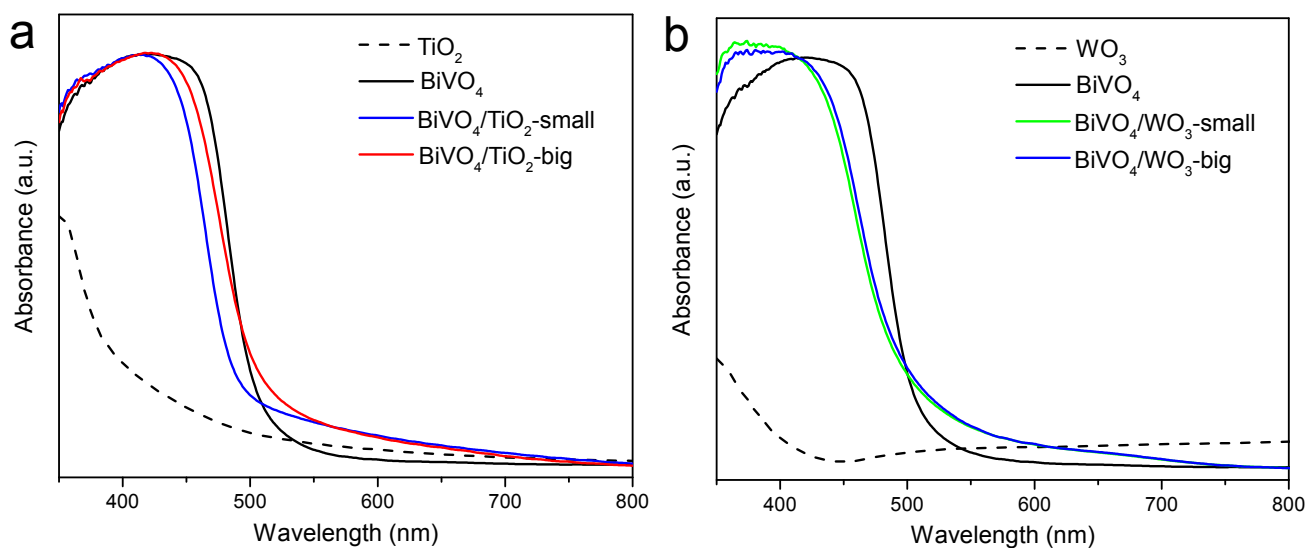


Figure S15. UV-Vis absorption spectra of (a) BiVO₄/TiO₂-small and BiVO₄/TiO₂-big and (b) BiVO₄/WO₃-small and BiVO₄/WO₃-big nanocomposites compared with bare BiVO₄, bare TiO₂, and bare WO₃. The BiVO₄/Al₂O₃ nanocomposites exhibited the same optical properties of the pure BiVO₄ film.

Table S1. Comparison of Bi : V molar ratio in the reaction mixture as precursors (first column), in the as-deposited NC films (second column) and after NaOH treatment (third column). Values reported in second and third column were derived by ICP-AES analysis.

Bi : V in reaction mixture	Bi : V in as-deposited films^a	Bi : V in films after NaOH^b
3:1	1:1.4	1:1
1:1	1:2.2	1:1
1:2	1:2.5	1:1

^a The samples were deposited on silicon and annealed at 500 °C for 10 min.

^b After annealing at 500 °C for 10 min, films were immersed in 1M NaOH solution for 30 sec to remove excess vanadium. The digestion was carried out in concentrated nitric acid.

Table S2. Fit parameters showing the % amplitude, the extracted lifetime, the fast, medium, and slow components of the different BiVO₄/MO nanocomposites compared with bare BiVO₄.

Nanocomposite	% Amplitude	Lifetime (ps)	Fast (ps)	Medium (ps)	Slow (ns)
BiVO ₄	19	64	50	11000	100
BiVO ₄ /Al ₂ O ₃	15	51	50	11000	100
BiVO ₄ /WO ₃ -small	42	12	7.5	160	7.6
BiVO ₄ /WO ₃ -big	35	19	7.0	154	9.2

- 1 P. D. Cozzoli, A. Kornowski, and H. Weller, *J. Am. Chem. Soc.*, **2003**, *125*, 14539.
- 2 R. Buonsanti, E. Carlino, C. Giannini, D. Altamura, L. De Marco, R. Giannuzzi, M. Manca, G. Gigli, and P. D. Cozzoli, *J. Am. Chem. Soc.*, **2011**, *133*, 19216.
- 3 T. M. Mattox, A. Bergerud, A. Agrawal, and D. J. Milliron, *Chem. Mater.*, **2014**, *26*, 1779.
- 4 K. Manthiram, and A. P. Alivisatos, *J. Am. Chem. Soc.*, **2012**, *134*, 3995.
- 5 H. Zhang, J. S. Sun, J. Jang, J.-S. Lee, W.-L. Ong, J. A. Malen, and D. V. Talapin, *ACS Nano*, **2013**, *7*, 10296.

- 6 L. Chen, E. Alarcón-Lladó, M. Hettick, I. D. Sharp, Y. Lin, A. Javey, and J. W. Ager, *J. Phys. Chem. C*, **2013**, *117*, 21635.
- 7 L. Leontie, M. Caraman, M. Alexe, and C. Harnagea, *Surface Science*, **2002**, *507*, 480;
- 8 A. Bergerud, R. Buonsanti, J. L. Lordan-Sweet, and D. Milliron, *Chem. Mater.*, **2013**, *15*, 3172.
- 9 A. Walsh, Y. Yan, M. N. Huda, M. Mowafak, A.-Jassim and S.-H. Wei, *Chem. Mater.*, **2009**, *21*, 547;
- 10 S. P. Berglund, A. J. E. Rettie, S. Hoang and C. B. Mullins, *Phys. Chem. Chem. Phys.*, **2012**, *14*, 7065.
- 11 Z. Zhao, Z. Li and Z. Zou, *Phys. Chem. Chem. Phys.*, **2011**, *13*, 4746.
- 12 J. K. Cooper, S. G. Gul, F. M. Toma, L. Chen, P.-A. Glans, J. Guo, J. W. Ager, J. Yano, I. D. Sharp, *Chem. Mater.*, **2014**, *26*, 5365.
- 13 J. K. Cooper, S. Gul, F. M. Toma, L. Chen, Y.-S Liu, J. Guo, J. W. Ager, J. Yano, I. D. Sharp, *J. Phys. Chem. C*, **2015**, *119*, 2969.